

# Characterization and Pseudo-Capacitance Performance of Porous Co<sub>3</sub>O<sub>4</sub> Nanorods Synthesized by Thermal Decomposition

Ruyi Zou<sup>1,2</sup>, Lin Zhu<sup>1</sup>, Lijun Yan<sup>1</sup>, Bo Shao<sup>1</sup>, Xiaoping Zhang<sup>1,\*</sup>, Wei Sun<sup>1,\*</sup>

<sup>1</sup> Key Laboratory of Laser Technology and Optoelectronic Functional Materials of Hainan Province, Key Laboratory of Functional Materials and Photoelectrochemistry of Haikou, College of Chemistry and Chemical Engineering, Hainan Normal University, Haikou 571158, P R China

<sup>2</sup> Jiangxi Province Key Laboratory of Polymer Preparation and Processing, School of Chemistry and Environmental Sciences, Shangrao Normal University, Shangrao 334001, China

\*E-mail: [sunwei@hainnu.edu.cn](mailto:sunwei@hainnu.edu.cn)

Received: 4 February 2020 / Accepted: 21 March 2020 / Published: 10 May 2020

---

Porous Co<sub>3</sub>O<sub>4</sub> nanorods were synthesized by the thermolysis of organometallic cobalt oxalate precursor via ultrasonic assisted method. FT-IR, XRD, XPS, SEM, TEM and BET were applied to characterize the effect of thermal treatment temperature on the properties of porous Co<sub>3</sub>O<sub>4</sub> nanorods. A three-electrode system was used to perform cyclic voltammetry, electrochemical impedance spectroscopy and galvanostatic charge-discharge measurements to study the electrochemical behaviours of Co<sub>3</sub>O<sub>4</sub> nanorods modified nickel foam electrodes. Compared with Co<sub>3</sub>O<sub>4</sub> prepared by pyrolysis at various temperatures, Co<sub>3</sub>O<sub>4</sub> nanorods obtained at 300 °C had the highest specific capacitance of 226.80 F·g<sup>-1</sup> at a current density of 1 A·g<sup>-1</sup> in the potential range of -0.4 to 0.6 V (vs. Hg/HgO). After performing 1000 cycles in 2 M KOH electrolyte, 99.76% of specific capacitance was retained, showing the excellent stability of Co<sub>3</sub>O<sub>4</sub> nanorods modified electrode.

---

**Keywords:** Cobalt oxide nanorods; Supercapacitor; Thermal decomposition; Pseudo-capacitance

## 1. INTRODUCTION

Supercapacitor is vital energy storage devices for intermittent renewable energy power generation technologies such as wind energy [1], solar energy [2], and tidal energy [3]. In recent decades, the researches on supercapacitors have mainly focused on the devising of novel electrode materials. Among them, Co<sub>3</sub>O<sub>4</sub> is considered as a potential electrode material not only because of its environmental friendliness and richness but also its large theoretical specific capacitance (3650 F·g<sup>-1</sup>) [4]. In practical applications, the poor electrical conductivity of Co<sub>3</sub>O<sub>4</sub> results in the lower specific capacitance than the theoretical value [5]. Therefore, various strategies such as doping [6], compounding [7] or morphology-

controlled synthesis [8] are devised to improve conductivity and surface properties with the specific capacitance enhanced. The specific capacitance of the electrode material is closely related to its specific surface area and pore size distribution, which is ascribed to the fact that the stored charge is depended on the Faraday redox reaction that occurred in the superficial layer of the material. Also, the high porosity of the electrode material can promote electrolyte diffusion and charge transfer, which can further improve the specific capacitance [9].

In this work,  $\text{Co}_3\text{O}_4$  nanorods were obtained by pyrolysis of rod-shaped cobalt oxalate precursors prepared by ultrasonic assisted synthesis method [10]. The organic components in the precursor were thermally decomposed to form the porous structure  $\text{Co}_3\text{O}_4$  nanorods. The influence of heat treatment temperature on the porosity of  $\text{Co}_3\text{O}_4$  was great during thermal decomposition of organic precursors or calcination of materials [11]. Excessive heating and sintering can cause grain size to increase with pore shrinkage, which would seriously damage the specific surface area of  $\text{Co}_3\text{O}_4$  material with its specific capacitance decreased. Different heat treatment temperatures were set to prepare a series of porous  $\text{Co}_3\text{O}_4$  nanorods with their properties characterized by various instruments and electrochemical methods.

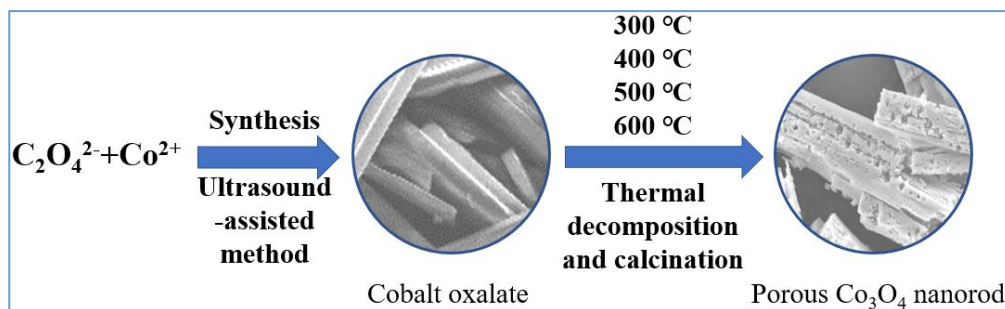
## 2. EXPERIMENTAL SECTION

### 2.1. Reagents

$\text{K}_2\text{C}_2\text{O}_4 \cdot \text{H}_2\text{O}$ , polyvinylidene fluoride (PVDF) and 1-methyl-2-pyrrolidone (NMP) were purchased from Aladdin Industrial Corporation.  $\text{Co}(\text{NO}_3)_2 \cdot 6\text{H}_2\text{O}$  (Sinopharm Chemical Reagent Co., Ltd.), nickel foam (Suzhou Lexiang Electronic Technology Co., Ltd.), acetylene black (Tianjin Xinglongtai Chemical Products Technology Co., Ltd.) were got without further purification and all aqueous solutions were prepared with distilled water.

### 2.2. Synthesis procedure

$\text{Co}_3\text{O}_4$  nanorods were synthesized through ultrasound-assisted method with detailed procedure as follows [10]. 80 mL of  $\text{K}_2\text{C}_2\text{O}_4$  solution (0.2 M) was slowly added to 50 mL of  $\text{Co}(\text{NO}_3)_2$  solution (0.3 M) with ultrasound irradiation (45 kHz and 60 W) for 30 min at room temperature. The pink precipitate was separated by centrifugation and washed with water for several times, which was dried in vacuum at 60 °C for 10 hours to obtain the precursor. Then the precursor was calcined in a muffle furnace (Hefei Kejing Materials Technology Co. Ltd., China) at different temperature (300, 400, 500 and 600 °C) for 3 h to obtain  $\text{Co}_3\text{O}_4$  nanorods (signed as III- $\text{Co}_3\text{O}_4$ , IV- $\text{Co}_3\text{O}_4$ , V- $\text{Co}_3\text{O}_4$ , and VI- $\text{Co}_3\text{O}_4$ ) with synthesis process shown in Scheme 1.



**Scheme 1.** Schematic illustration of the fabrication of porous  $\text{Co}_3\text{O}_4$  nanorods.

### 2.3. Material characterizations

The phase structure was checked by powder X-ray diffraction (XRD) on a Miniflex II apparatus (Rigaku, Japan) equipped with  $\text{Cu-K}\alpha$  radiation ( $\lambda = 0.15418$  nm). The morphologies were observed by JSM-7100F field emission scanning electron microscopy (SEM, JEOL, Japan) and JEM-2100F High-resolution transmission electron microscopy (HRTEM, JEOL, Japan). Fourier transform-infrared (FT-IR) spectrum was measured on a Nicolet 6700 FT-IR spectrophotometer (Thermo Fisher Scientific Inc., USA). X-ray photoelectron spectrometer (XPS, Axis Supra, Shimadzu Kratos, Japan) was implemented with  $\text{Al-K}\alpha$  as the excitation source. Thermogravimetry-differential scanning calorimetry (TG-DSC) measurements of the precursor was performed on STA 449 F3 Jupiter thermogravimetric analyzer (Netzsch Instruments, Germany) with a heating rate of  $10$  °C  $\text{min}^{-1}$  in flowing  $\text{N}_2$  from  $30$  to  $600$  °C. Adsorption isotherms were measured with a Quantachrome Autosorb-iQ gas adsorption analyzer (Quantachrome Instruments, USA). Electrochemical properties were evaluated using an Autolab PGSTAT 302N electrochemical workstation (Metrohm, Switzerland).

### 2.4. Electrochemical investigations

The  $\text{Co}_3\text{O}_4$  nanorods based working electrode was prepared with the following steps. Typically, 80 wt%  $\text{Co}_3\text{O}_4$  nanorods powder, 10 wt % acetylene black (as conducting agent) and 10 wt % PVDF (as binder) were uniformly mixed. Then NMP was added to prepare a slurry, which was then coated on nickel foam ( $1$  cm  $\times$   $1$  cm), dried at  $90$  °C for 10 hours, and then pressed to get an electrode at a pressure of 8 MPa [12].

Electrochemical properties of  $\text{Co}_3\text{O}_4$  nanorods modified electrode were examined by galvanostatic charge-discharge (GCD), cyclic voltammetry (CV) and electrochemical impedance spectroscopy (EIS) in a three-electrode cell with as-prepared electrode, platinum wire electrode and  $\text{Hg/HgO}$  electrode as working, counter and reference electrode, respectively, and 2 M KOH as the electrolyte. CV tests were performed in the electrochemical window of  $-0.5$ ~ $0.7$  V at different scan rates. GCD experiments were done between  $-0.4$  and  $0.6$  V at different electric current density. EIS were performed at a superimposed 5 mV sinusoidal voltage with frequency range of  $10^2$  kHz~ $0.01$  Hz.

### 3. RESULTS AND DISCUSSIONS

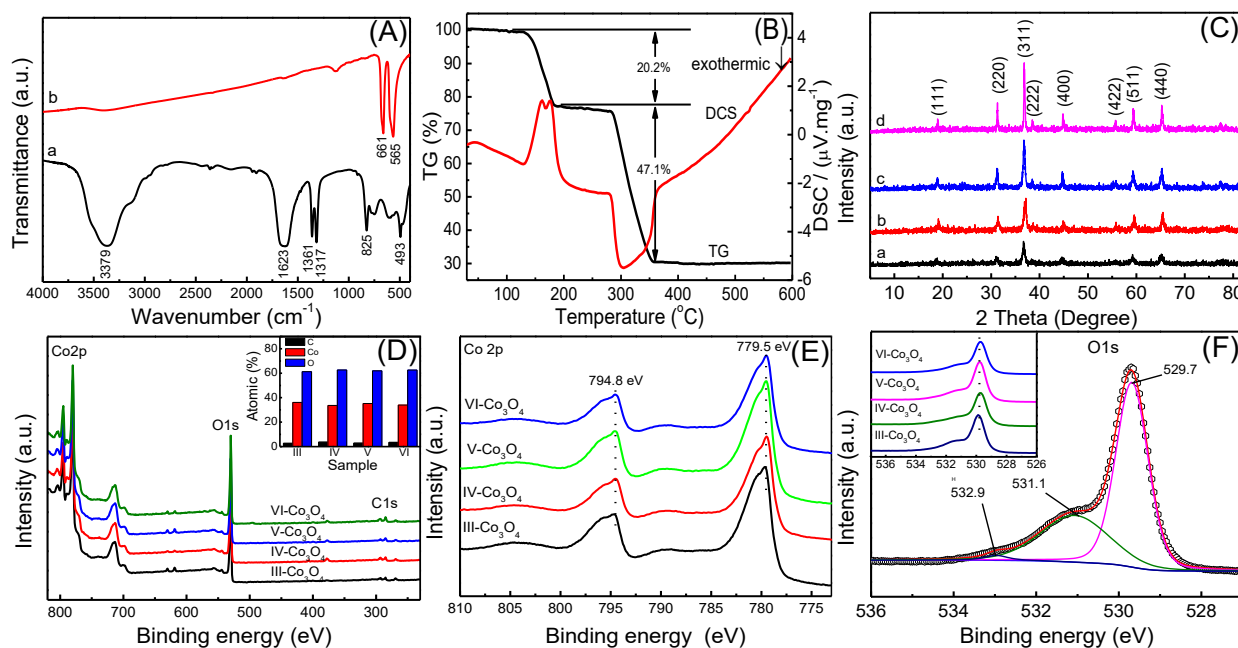
#### 3.1. Structural and morphological characterization

Figure 1A showed the FT-IR spectra of the precursor (curve a) and III-Co<sub>3</sub>O<sub>4</sub> (curve b). On curve a the typical bands of cobalt oxalate could be observed clearly, which was consistent with literature [13]. On curve b only two bands at 661 cm<sup>-1</sup> (the characteristic vibration of Co<sup>3+</sup>-O in octahedral coordination of Co<sub>3</sub>O<sub>4</sub> lattice) and 565 cm<sup>-1</sup> (vibration of Co<sup>2+</sup>-O in tetrahedral coordination) could be found [12,14], which was the typical data of Co<sub>3</sub>O<sub>4</sub>.

As shown in Figure 1B, thermogravimetric analysis (TG) of precursor was carried out with two distinct weight loss steps appeared. The first weight loss at 150~190 °C was corresponded to the evaporation of structural water of precursor with 20.2% weight lost, which was close to the mass ratio (19.7%) of two water molecules in one molecule of CoC<sub>2</sub>O<sub>4</sub>·2H<sub>2</sub>O. The second weight loss at 280~360 °C with an exothermal peak in the DSC curve could be ascribed to conversion of anhydrous cobalt oxalate to cobalt metal with weight loss (47.1%) close to the theoretical value (48.1%), proving the reaction equation as CoC<sub>2</sub>O<sub>4</sub> → Co + 2CO<sub>2</sub>↑ [15,16]. After the temperature exceeded 360 °C, the TG curve extended horizontally and the DSC curve extended obliquely upward, which indicated that the product of thermal decomposition absorbed heat for the phase transition without material loss.

Figure 1C presented the XRD pattern of Co<sub>3</sub>O<sub>4</sub> nanorods with peaks located at 2θ of 18.93°, 31.20°, 36.78°, 44.75°, 59.32° and 65.29°, which was matched well with the pure cubic phase of Co<sub>3</sub>O<sub>4</sub> spinel (JCPDS 42-1467) [17,18]. With the increase of calcination temperature from 300 °C to 600 °C, the higher crystallinity of Co<sub>3</sub>O<sub>4</sub> nanorods could be formed with the intensity of diffraction peaks getting stronger. No other peaks for impurities can be detected. Conversely, III-Co<sub>3</sub>O<sub>4</sub> retained more amorphous characteristic than other samples processed at high temperatures, which improved the wettability of Co<sub>3</sub>O<sub>4</sub> with abundant heterogeneous crystal defects [19]. In addition, the Scherrer equation ( $D = 0.9\lambda/\beta\cos\theta$ ) [20] can be used to estimate the average grain size of Co<sub>3</sub>O<sub>4</sub> as 8.0, 30.1, 44.1, and 63.3 nm, respectively, which indicated that the higher the calcination temperature, the larger the particle size of Co<sub>3</sub>O<sub>4</sub> microcrystals.

Figure 1D showed XPS survey spectra of Co<sub>3</sub>O<sub>4</sub> nanorods and the peaks located at 285 eV, 530 eV and 780 eV were the characteristic peaks of C 1s, O 1s and Co 2p, respectively. According to the XPS data, atomic percentages of C (2.7~3.48 %), Co (36.07~33.93 %) and O (61.23~62.59%) could be reached (Figure 1D inset). Figure 1E displayed the typical Co 2p XPS spectra of Co<sub>3</sub>O<sub>4</sub>. Two major peaks at 794.8 eV and 779.5 eV were corresponded to the Co 2p<sub>1/2</sub> and Co 2p<sub>3/2</sub> spin-orbit peaks of the Co<sub>3</sub>O<sub>4</sub> phase [21] with the energy separation as 15.3 eV. The O 1s core level spectrum (Figure 1F) showed three distinct components, in which the O 1s peaks at 532.9 and 531.1eV were oxygen atoms in hydroxyl groups and absorbed water, and the strong peak at 529.7 eV was oxygen atoms in Co<sub>3</sub>O<sub>4</sub> [22,23].



**Figure 1.** (A) FT-IR spectrum of precursor (a) and III- $\text{Co}_3\text{O}_4$  (b), (B) TG-DSC curves of precursor, (C) XRD patterns of III- $\text{Co}_3\text{O}_4$  (a); IV- $\text{Co}_3\text{O}_4$  (b); V- $\text{Co}_3\text{O}_4$  (c) and VI- $\text{Co}_3\text{O}_4$  (d), (D) XPS survey spectra of as-prepared  $\text{Co}_3\text{O}_4$  nanorod (inset: chart showing the percentages of carbon, cobalt and oxygen according to XPS data); (E) XPS core level spectra of Co 2p (F) and O 1s of as-prepared  $\text{Co}_3\text{O}_4$  nanorod.

The morphology and microstructure of the precursor and four  $\text{Co}_3\text{O}_4$  nanorods were observed by SEM. As can be seen from Figure 2 (A→E), all of them appeared as rods-like rectangular cross sections with distinct differences of surface morphology. The surface of the precursor was smooth (Figure 2A), while the surfaces of III- $\text{Co}_3\text{O}_4$  (Figure 2B) and IV- $\text{Co}_3\text{O}_4$  (Figure 2C) were rough with fine particles arranged in order along the long axis of the square-section rods. The surface of VI- $\text{Co}_3\text{O}_4$  (Figure 2E) looked like the surface of Bitter Gourd (*Momordica charantia L.*) with nodules and gullies, which were formed by the crystals on VI- $\text{Co}_3\text{O}_4$  surface fused at high temperature and then congealed after cooling. When the calcination temperature was 500 °C, the surface of V- $\text{Co}_3\text{O}_4$  nanorods had dual morphologies of IV- $\text{Co}_3\text{O}_4$  and VI- $\text{Co}_3\text{O}_4$  (Figure 2D), indicating that the fusion of  $\text{Co}_3\text{O}_4$  nanocrystal lines had begun to exacerbate at 500 °C. Figure 2F was the HRTEM image of III- $\text{Co}_3\text{O}_4$ , where the parallel stripes with spacing of 0.45, 0.28 and 0.24 nm corresponded to (111), (220) and (311) crystal planes of spinel  $\text{Co}_3\text{O}_4$  [24,25].

The specific surface area and pore distribution of  $\text{Co}_3\text{O}_4$  nanorods were estimated by Brunauer-Emmet-Teller (BET) and Barret-Joyner-Halender (BJH) method. Figure 3 showed the adsorption/desorption isotherms and the corresponding pore size distribution plots. Type IV isotherms and type H3 hysteresis loops for mesoporous materials could be observed with the specific surface areas and pore volumes of these  $\text{Co}_3\text{O}_4$  nanorods exhibited in Table 1. The increase of temperature of the calcined sample led to the decrease of the specific surface area of the samples with the recrystallization and growth of nanocrystals [26], and III- $\text{Co}_3\text{O}_4$  had the largest specific surface area.

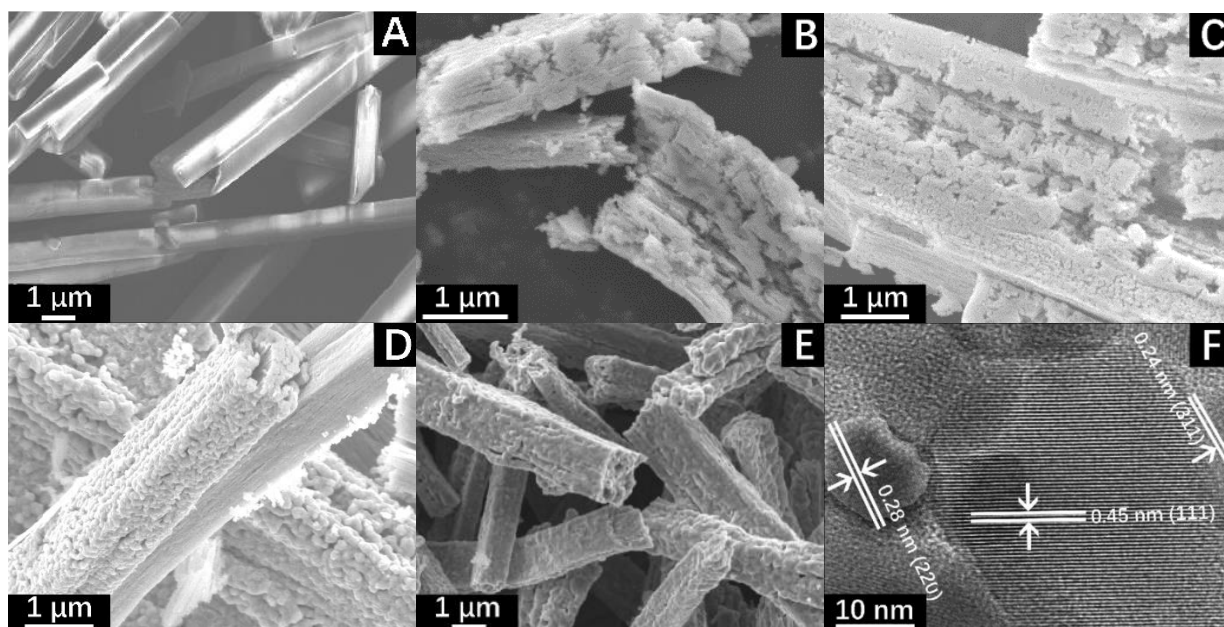


**Figure 2.** SEM images of precursor (A), III-Co<sub>3</sub>O<sub>4</sub> (B), IV-Co<sub>3</sub>O<sub>4</sub> (C), V-Co<sub>3</sub>O<sub>4</sub> (D), VI-Co<sub>3</sub>O<sub>4</sub> (E); HRTEM image of III-Co<sub>3</sub>O<sub>4</sub> (F).

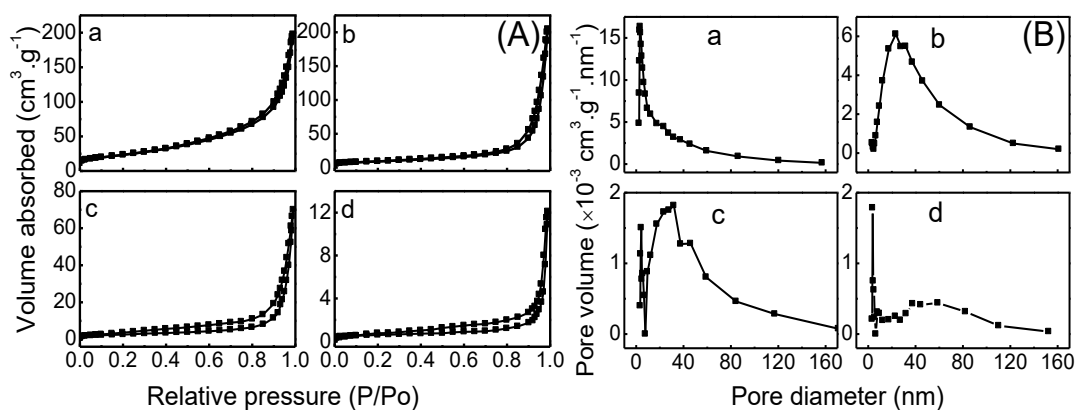


**Figure 3.** (A) N<sub>2</sub> adsorption-desorption isotherms and (B) pore size distribution curves of III-Co<sub>3</sub>O<sub>4</sub> (a), IV-Co<sub>3</sub>O<sub>4</sub> (b), V-Co<sub>3</sub>O<sub>4</sub> (c) and VI-Co<sub>3</sub>O<sub>4</sub> (d).

**Table 1** Calcining temperature and the related parameters of Co<sub>3</sub>O<sub>4</sub> nanorods

Sample	Calcination temperature (°C)	Specific surface area (m <sup>2</sup> ·g <sup>-1</sup> )	Pore volume (cm <sup>3</sup> ·g <sup>-1</sup> )	Pore diameter (nm)
III-Co <sub>3</sub> O <sub>4</sub>	300	82.704	0.339	3.409
IV-Co <sub>3</sub> O <sub>4</sub>	400	41.135	0.320	23.369
V-Co <sub>3</sub> O <sub>4</sub>	500	14.670	0.108	31.828
VI-Co <sub>3</sub> O <sub>4</sub>	600	2.519	0.019	3.8146

### 2.2 Electrochemical measurements

Electrochemical performance of the Co<sub>3</sub>O<sub>4</sub> nanorods based electrode was studied by different electrochemical techniques. As shown in Figure 4A, CV curves of Co<sub>3</sub>O<sub>4</sub> nanorod electrode gave two

pairs of redox peaks (P1/P2 and P3/P4) in each CV curve, which were attributed to the conversion of  $\text{Co}^{2+}/\text{Co}^{3+}$  and  $\text{Co}^{3+}/\text{Co}^{4+}$  with the possible following reaction mechanisms [27]:



Also III- $\text{Co}_3\text{O}_4$  based electrode showed the largest integrated area in cyclic voltammogram, which was due to its larger specific surface and higher porosity [28]. The specific capacitances at different scan rates were calculated from the following equation  $C_m = [IdV]/(2vm\Delta V)$  [29] with the variational tendency of the specific capacitances shown in Figure 4B, which indicated that the increase of scan rate resulted in the decrease of the specific capacitance.

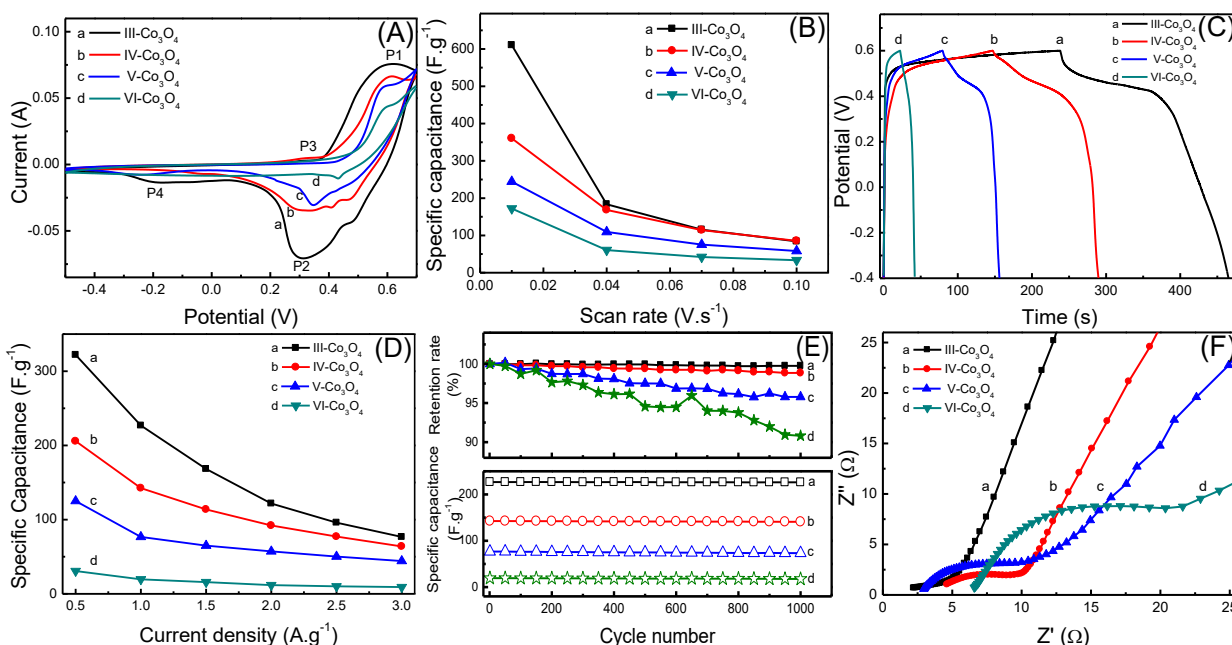


**Figure 4.** (A) CV curves at the scan rate of  $10 \text{ mV}\cdot\text{s}^{-1}$  and (B) Variation of specific capacitances with respect to scan rate of 10, 40, 70 and  $100 \text{ mV}\cdot\text{s}^{-1}$  of III- $\text{Co}_3\text{O}_4$  (a), IV- $\text{Co}_3\text{O}_4$  (b), V- $\text{Co}_3\text{O}_4$  (c) and VI- $\text{Co}_3\text{O}_4$  (d) base electrode; (C) GCD curves at the current density of  $1.0 \text{ A}\cdot\text{g}^{-1}$ ; (D) variation of specific capacitances at different current densities of 0.5, 1.0, 1.5, 2.0, 2.5 and  $3.0 \text{ A}\cdot\text{g}^{-1}$ ; (E) specific capacitance and retention ratio variation within 1000 GCD cycles at the current density of  $1.0 \text{ A}\cdot\text{g}^{-1}$ ; (F) Nyquist curves of III- $\text{Co}_3\text{O}_4$  (a), IV- $\text{Co}_3\text{O}_4$  (b), V- $\text{Co}_3\text{O}_4$  (c) and VI- $\text{Co}_3\text{O}_4$  (d) electrode in the solution of 2 M KOH.

Figure 4C showed the charge-discharge curves of  $\text{Co}_3\text{O}_4$  nanorods based electrodes at  $1.0 \text{ A}\cdot\text{g}^{-1}$  in 2 M KOH. The charging platform at approximately 0.53 V and the discharge platform at 0.44 V corresponded to the reduction and the oxidation process, which was attributed to pseudo-capacitance resulting from faradic reaction [30]. Also in curve (a) longest time of charge-discharge could be observed, which indicated that III- $\text{Co}_3\text{O}_4$  possessed the largest specific capacitance at  $1.0 \text{ A}\cdot\text{g}^{-1}$ . According to the equation  $C_m = Idt/m\Delta V$  [31], the capacitance of III- $\text{Co}_3\text{O}_4$ , IV- $\text{Co}_3\text{O}_4$ , V- $\text{Co}_3\text{O}_4$  and VI- $\text{Co}_3\text{O}_4$  electrode at current density of  $1.0 \text{ A}\cdot\text{g}^{-1}$  were calculated as 226.80, 142.46, 76.72 and  $19.61 \text{ F}\cdot\text{g}^{-1}$ , indicating that the high-temperature calcination led to a decrease in the specific capacitance [32]. Table 2 listed the comparisons of the specific capacitance of various  $\text{Co}_3\text{O}_4$  based electrode at  $1 \text{ A}\cdot\text{g}^{-1}$ , which indicated that the values were greatly influenced by the morphology. Figure 4D showed the variation of

specific capacitances of each electrode at different current densities, which decreased with increasing current density due to the charge-discharge time limited the redox reaction of  $\text{Co}_3\text{O}_4$  [33].

**Table 2** Specific capacitance with various morphologies  $\text{Co}_3\text{O}_4$  based electrodes at  $1 \text{ A}\cdot\text{g}^{-1}$ .

Morphology	Electrolyte	C ( $\text{F}\cdot\text{g}^{-1}$ )	Potential window (V)	Ref
Hollow boxes	3% KOH	216	0~0.50	[34]
Layered	2 M KOH	202.5	0 ~ 0.40	[35]
Nanoneedles	2 M KOH	201.3	0~0.55	[36]
Nanosheet	2 MKOH	176.8	0~0.50	[37]
Scroll	6 M KOH	12.9	0~0.40	[38]
Particles	2 M KOH	150	0~0.50	[39]
Tubes	3 M KOH	128.3	0~0.45	[40]
Nanorods	2 M KOH	226.80	-0.4~0.6	This work

Galvanostatic cycling stability were carried out at current density of  $1.0 \text{ A}\cdot\text{g}^{-1}$  for 1000 cycles. Figure 4E showed the specific capacitance variation for  $\text{Co}_3\text{O}_4$  nanorods modified electrodes, and the capacitance retention rates of III- $\text{Co}_3\text{O}_4$ , IV- $\text{Co}_3\text{O}_4$ , V- $\text{Co}_3\text{O}_4$  and VI- $\text{Co}_3\text{O}_4$  electrodes were 99.76%, 98.85%, 95.79% and 90.81%, respectively. The III- $\text{Co}_3\text{O}_4$  electrode had the highest capacitance retention rate due to its relative best microstructure.

EIS measurements were used to demonstrate the interfacial performance and Figure 4F exhibited Nyquist plots of III- $\text{Co}_3\text{O}_4$  (a), IV- $\text{Co}_3\text{O}_4$  (b), V- $\text{Co}_3\text{O}_4$  (c), and VI- $\text{Co}_3\text{O}_4$  (d) electrodes. The values of these intercepts were 2.2, 4.6, 2.9 and 6.6  $\Omega$ , which corresponded to the equivalent series resistance values of the III- $\text{Co}_3\text{O}_4$ , IV- $\text{Co}_3\text{O}_4$ , V- $\text{Co}_3\text{O}_4$ , and VI- $\text{Co}_3\text{O}_4$  electrodes, respectively. The value of the charge transfer resistance ( $R_{ct}$ ) were got as 2.6, 5.1, 7.0 and 13.8  $\Omega$ . The increase of  $R_{ct}$  value indicated that the interfacial resistance increased, which could be attributed to the increase of the calcination temperature leading to the decrease of the specific surface area with gradual loss of the pore structure.

#### 4. CONCLUSIONS

Cobalt oxalate precursor was thermally decomposed to obtain porous  $\text{Co}_3\text{O}_4$  nanorods at different temperatures. The results indicated that the product heat-treated at  $300 \text{ }^\circ\text{C}$  had a large specific surface area and rich porosity with more amorphous components. III- $\text{Co}_3\text{O}_4$  base electrode performed quasi-reversible redox reactions in 2 M KOH electrolyte with the specific capacitances of  $226.80 \text{ F}\cdot\text{g}^{-1}$  at a current density of  $1.0 \text{ A}\cdot\text{g}^{-1}$ . After 1000 GCD cycle tests, 99.76% of capacitance were still retained. All the results indicated that III- $\text{Co}_3\text{O}_4$  nanorods electrode had the best electrochemical performance.

#### ACKNOWLEDGEMENTS

This work was financially supported by the Key Science and Technology Program of Haikou City (2017042) and the Graduate Student Innovation Research Project of Hainan Province (Hsyx2017-11).

#### References

1. F. Q. Xu, J. C. Liu, S. S. Lin, Q. G. Dai and C. B. Li, *Energy*, 163 (2018) 585.
2. A. Q. Al-Shetwi, M. Z. Sujod and F. Blaabjerg, *Sol. Energy*, 159 (2018) 665.
3. M. C. Sousounis, J. K. H. Shek and B. G. Sellar, *J. Energy Storage*, 21 (2019) 445.
4. H. R. Barai, N. S. Lopa, P. Barai, M. M. Rahman, A. K. Sarker, and S. W. Joo, *J. Mater. Sci-Mater. El.*, 30 (2019) 21269.
5. X. Y. Deng, J. J. Li, S. Zhu, F. He, C. N. He, E. Z. Liu, C. S. Shi, Q. F. Li and N. Q. Zhao, *J. Alloy. Compd.*, 693 (2017) 16.
6. S. J. Deng, X. C. Xiao, G. Chen, L. H. Wang and Y. D. Wang, *Electrochim. Acta*, 196 (2016) 316.
7. B. Wang, Y. Wang, J. Park, H. Ahn and G. X. Wang, *J. Alloys. Compd.*, 509 (2011) 7778.
8. K. Deori, S. K. Ujjain, R. K. Sharma and S. Deka, *ACS Appl. Mater. Inter.*, 5 (2013) 10665.
9. J. C. Huang, J. T. Zhu, K. Cheng, Y. Xu, D. X. Cao and G. L. Wang, *Electrochim. Acta*, 75 (2012) 273.
10. D. Xie, X. M. Du, Q. M. Su, W. W. Yuan, Z. M. Dong, J. Zhang and G. H. Du, *Appl. Phys. A*, 118 (2015) 1171.
11. J. Zheng, J. Liu, D. Lv, K. Qin, Z. Jiang, Z. Xie, R. Huang and L. Zheng, *J. Solid. State. Chem.*, 183 (2010) 600.
12. H. Adhikari, M. Ghimire, C. K. Ranaweera, S. Bhoyate, R. K. Gupta, J. Alam and S. R. Mishra, *J. Alloy. Compd.*, 708 (2017) 628.
13. B. M. Abu-Zied, S. M. Bawaked, S. A. Kosa and W. Schwieger, *Appl. Surf. Sci.*, 351 (2015) 600.
14. R. Y. Zou, L. Zhu, G. L. Luo, Y. Y. Niu, H. Xie, R. X. Dong, H. Cheng, W. Sun and L. J. Zhang, *Int. J. Electrochem. Sci.*, 15 (2020) 484.
15. J. Qi, W. Zhang and R. Cao, *Chem. Commun.*, 53 (2017) 9277.
16. D. Lützenkirchen-Hecht, J. D. Grunwaldt, M. Richwin, B. Griesebock, A. Baiker and R. Frahm, *Phys Scripta*, 2005 (2005) 831.
17. Z. Y. Pu, H. Zhou, Y. F. Zheng, W. Z. Huang and X. N. Li, *Appl. Surf. Sci.*, 410 (2017) 14.
18. J. González-Prior, R. López-Fonseca, J. I. Gutiérrez-Ortiz and B. D. Rivas, *Appl. Catal. B-environl*, 199 (2016) 384.
19. C. J. Liu, X. Y. Feng, N. Li, C. W. Luo and Z. S. Chao, *Surf. Coat. Tech.*, 309 (2017) 1111.
20. Q. M. Ren, Z. T. Feng, S. P. Mo, C. L. Huang, S. J. Li, W. X. Zhang, L. M. Chen, M. L. Fu, J. L. Wu and D. Q. Ye, *Catal. Today*, 332 (2019) 160.
21. X. Chen, C. Zhong, B. Liu, Z. Liu, X. X. Bi, N. Q. Zhao, X. P. Han, Y. D. Deng, J. Lu and W. B. Hu, *Small* 14 (2018) 1702987.
22. L. Xu, Y. Q. Zou, Z. H. Xiao and S. Y. Wang, *J. Energy Chem.*, 35 (2019) 24.
23. M. Cordoba, C. Miranda, C. Lederhos, F. Coloma-Pascual, A. Ardila, G. A. Fuentes, Y. Pouilloux and A. Ramírez, *Catalysts*, 7 (2017) 384.
24. C. Su, L. Zhang, Y. T. Han, X. W. Chen, S. T. Wang, M. Zeng, N. T. Hu, Y. J. Su, Z. H. Zhou, H. Wei, H. Wei and Z. Yang, *Sensor. Actuat. B-Chem.*, 288 (2019) 699.
25. L. M. Liu, T. Li, Z. C. Yi, F. Chi, Z. D. Lin, X. W. Zhang and K. Xu, *Sensor. Actuat. B-Chem.*, 297 (2019) 126815.
26. Y. J. Zhao, X. M. Xu, Y. Z. Zhao, H. P. Zhou, J. B. Li, H. B. Jin, *J. Alloy. Compd.*, 654 (2016) 523.
27. S. A. Pawar, D. S. Patil and J. C. Shin, *J. Ind. Eng. Chem.*, 54 (2017) 162.
28. Y. Lin, Q. Wang, S. Y. Gao, H. B. Yang and P. Liu, *Ceram. Int.*, 44 (2018) 2649.
29. Y. Y. Lan, H. Y. Zhao, Y. Zong, X. H. Li, Y. Sun, J. Feng, Y. Wang, X. L. Zheng and Y. P. Du, *Nanoscale*, 10 (2018) 11775.
30. Rusi and S. R. Majid, *Electrochim. Acta*, 175 (2015) 193.
31. L. Y. Xu, L. Y. Zhang, B. Cheng and J. G. Yu, *Carbon*, 152 (2019) 652.
32. J. L. Chen, Z. F. Xu, H. L. Zhu, R. Liu, X. J. Song, Q. Song, J. Wu, C. Z. Zhang, L. Ding, J. L. Dong and H. Z. Cui, *Vacuum*, 174 (2020) 109219.
33. R. Packiaraj, P. Devendran, K. S. Venkatesh, S. Asath bahadur, A. Manikandan and N. Nallamuthu,

- J. Supercond. Nov. Mag.*, 32 (2019) 2427.
34. W. Du, R. M. Liu, Y. W. Jiang, Q. Y. Lu, Y. Z. Fan and F. Gao, *J. Power Sources*, 227 (2013) 101.
  35. D. W. Wang, Q. H. Wang and T. M. Wang, *Inorg. Chem.*, 50 (2011) 6482.
  36. G. G. Li, M. Z. Chen, Y. Ouyang, and D. Yao, L. Lu, L. Wang, X. F. Xia, W. Lei, S. M. Chen, D. Mandler and Q. L. Hao, *Appl. Surf. Sci.*, 469 (2019) 941.
  37. Y. Wang, Z. Y. Zhong, Y. Chen, C. T. Ng and J. Y. Lin, *Nano. Res.*, 4 (2011) 695.
  38. W. W. Zhou, J. P. Liu, T. Chen, K. S. Tan, X. T. Jia, Z. Q. Luo, C. X. Cong, H. P. Yang, C. M. Li and T. Yu, *Phys. Chem. Chem. Phys.*, 13 (2011) 14462.
  39. F. L. Meng, Z. G. Fang, Z. X. Li, W. W. Xu, M. J. Wang, Y. P. Liu, J. Zhang, W. R. Wang, D. Y. Zhao and X. H. Guo., *J. Mater. Chem. A*, 1 (2013) 7235.
  40. D. L. Yan, H. Zhang, L. Chen, G. S. Zhu, S. C. Li, H. R. Xu and A. B. Yu, *ACS Appl. Mater. Inter.*, 6 (2014): 15632.

© 2020 The Authors. Published by ESG ([www.electrochemsci.org](http://www.electrochemsci.org)). This article is an open access article distributed under the terms and conditions of the Creative Commons Attribution license (<http://creativecommons.org/licenses/by/4.0/>).